

Look Both Ways: Bidirectional Visual Sensing for Automatic Multi-Camera Registration

Subodh Mishra*, Sushruth Nagesh, Sagar Manglani, Graham Mills**,
Punarjay Chakravarty and Gaurav Pandey

Abstract— This work describes the automatic registration of a large network (≈ 40) of fixed, ceiling-mounted environment cameras spread over a large area ($\approx 800 m^2$) using a mobile calibration robot equipped with a single upward-facing fisheye camera and a backlit ArUco marker for easy detection. The fisheye camera is used to do visual odometry (VO), and the ArUco marker facilitates easy detection of the calibration robot in the environment cameras. In addition, the fisheye camera is also able to detect the environment cameras. This two-way, bidirectional detection constrains the pose of the environment cameras to solve an optimization problem. Such an approach can be used to automatically register a large-scale multi-camera system used for surveillance, automated parking, or robotic applications. This VO based multicamera registration method is extensively validated using real-world experiments, and also compared against a similar approach which uses an LiDAR - an expensive, heavier and power hungry sensor.

Index Terms— Multi-camera registration, infrastructure-enabled autonomy.

I. INTRODUCTION



Fig. 1: **Edge nodes**: We perform experiments with a distributed sensing system of ~ 40 edge devices mounted throughout the ceiling of our test environment. Each edge node comprises of an RGB camera (we call it as environment camera in the paper) and compute. These are powered over ethernet and networked and time-synced to a central server.

Infrastructure Enabled Autonomy [1] is gaining popularity with the aim to equip the environment of an autonomous system with sensors that can eliminate the dependence on

*S. Mishra (subodh514@tamu.edu) is with Texas A&M University (work done as intern), others are with Ford Greenfield Labs, Palo Alto and can be reached at snagesh1@ford.com, smanglan@ford.com, pchakra5@ford.com, gpandey2@ford.com

**This work was performed by G. Mills (grayhem@gmail.com) when they were employed at Ford.

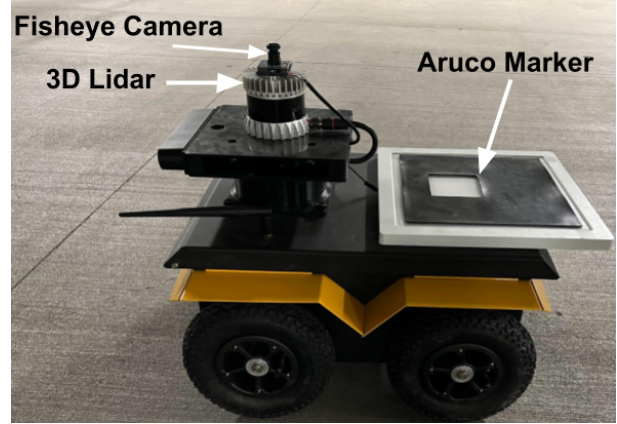


Fig. 2: **Calibration Robot**: Clearpath Jackal with an upward-facing wide-angle fisheye camera F and an ArUco marker M . The ArUco marker is backlit to make detection easier. The robot also carries a LiDAR for comparison between LiDAR and camera-only calibration.

onboard sensors for perception and localization, especially in controlled environments like parking lots, warehouses, and the factory floor. A distributed sensing system in a parking lot can autonomously park vehicles with drive-by-wire technology and direct the movement of cars through the environment. However, for such a network of fixed environment cameras to be useful to an autonomous robot for the aforementioned applications, they need to be registered w.r.t. each other such that the 6 DoF pose of each environment camera is known w.r.t. other environment cameras and ultimately w.r.t. a common frame of reference. A tedious way to determine the camera poses would involve detecting a calibration target (ArUco/Checkerboard) [2] in the common FoV between every pair of environment cameras, determining their relative poses and subsequently daisy-chaining the poses through the sequence of cameras and back to the starting camera. This approach would require significantly overlapping field of view (FoV) that cannot always be guaranteed in many practical scenarios, and tiresome manual labor when a large number of cameras need to be registered over a large area.

II. RELATED WORK

The automatic identification of the relationship between multiple fixed cameras in a network has been done in terms of the network topology by [3], [4]. However, this is used for the detection and re-id of people being tracked through

these cameras. One of the first works to describe the joint calibration of a system of surveillance cameras and a mobile robot [5] used homography between the image plane of each camera and the ground plane to calibrate the two. As the robot moved around the FoV of each camera, its simultaneous detection in the camera image plane and localization using LiDAR on the ground plane allowed the automated computation of homography between each camera and the ground plane. More recently, Zou et. al. [6] describe a set of fisheye cameras deployed at an intersection to monitor traffic. Each camera-node (comprising of sensor and compute) is extrinsically calibrated using homography between hand-picked points on the road (visible in the camera image) that are also discernible in a satellite image of the area. [7] describes a method to register a single fisheye camera in a given map, but, as the title suggests the method requires the foreknowledge of prior mapping data. Registration of multiple cameras with over-lapping fields of view is an easier problem to solve, for example by using Epipolar geometry. A comprehensive account of challenges in registration of multiple cameras with no or minimal common field of view is presented in [8]. [9] & [10] present methods of camera registration in which static non overlapping cameras track pedestrians and in the process determine the registration between 4 & 6 cameras respectively spread over a small area. Similarly, [11] presents a Kalman Filter based method to register 4 static cameras in the same plane by using trajectory estimation of a target in an area of $\approx 16 m^2$. [9], [10] and [11] are similar in their approach of tracking an object to determine metric topology of a network of cameras but these experiments have been carried out for small number of cameras and in a small area. [12] uses a RGB-D SLAM [13] to generate a prior map of 3D-points with visual intensity information, and then performs registration of 3 static non over-lapping cameras in it by 2D-3D correspondences followed by solving a PnP problem. [14] presents a method to register only two non over-lapping cameras that are less than a meter apart and rely heavily on the odometry of the calibration robot which comes from a wheel encoder like sensor that may not only drift but cannot be used for loop closures. [15] presents a technique where they register 2 static non over-lapping cameras. In this case the cameras to be registered need to have fiducial markers on them. The system requires a support calibration camera that can view the fiducial markers on the cameras to be registered and two different checkerboard targets simultaneously. This system will give precise registration results for small system of cameras but has practical limitations on extending it to a system of several cameras spread over a large area. For the scenario presented in [15], registering just 2 cameras not only required 1 support camera but also 4 fiducial markers in total making this system impractical for large scale large area registration. Unlike [12] that registers cameras in a prior RGB-D map, [16] registers 6 static non over-lapping cameras using a sparse 3D map obtained from a Visual SLAM [17] pipe-line by using selection manual 2D-2D correspondences between the SLAM camera and the environment camera. The

limitation of [16] is that it is not in metric scale, it requires manual selection of features and the mapping camera and the environment camera must capture images of the same area feature rich area - which is not possible in our scenario where the cameras to be calibrated look vertically below on a largely texture less surface which is not suitable for doing visual odometry/SLAM. [18] presents a technique to register 5 static RGB-D cameras out of which some share field of view and some do not. The process bridges camera poses by visual odometry in which the visual odometry camera and the RGB-D cameras need to co detect several fiducial markers in the scene, lastly a depth based refinement process is undertaken as RGB-D sensors also provide depth information. The shortcomings of this process is that it requires almost as many fiducial markers as the number of RGB-D cameras to be calibrated and these fiducial markers also should be co-detected in the visual odometry and the cameras being registered, this is practically not possible in scenarios involving a large number of cameras spread over a large area.

III. CONTRIBUTIONS

In this work, we present an approach to automatically register a large network (≈ 40) of static ceiling-mounted environment RGB cameras (Figures 1 & 3) with minimal or no overlap between them, spread over a large area ($\approx 800 m^2$) using a calibration robot (Figure 2) equipped with a single upward looking fisheye camera - for visual odometry (VO) [19] & detection of environment cameras (Figure 3), and a single back-lit ArUco marker - for easy detection of calibration robot in environment cameras (Figure 4). We use VO and ArUco marker detection to bridge the pose between environment cameras. We look and sense in both directions: downwards from each of the environment camera down onto the robot (as it passes through its FoV, Figure 4) and, upwards from the robot to the environment camera (Figure 3) to determine the pose of each environment camera relative to a common coordinate frame.

IV. SYSTEM DESCRIPTION & NOTATION

A. The Distributed Camera System

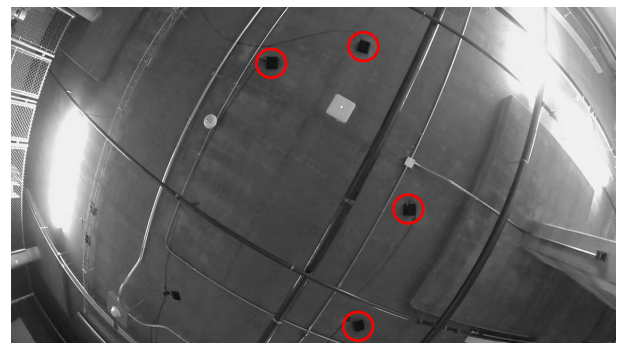


Fig. 3: **Looking up ↑ Edge-Node detection from Robot:** Automated detection of ceiling-mounted environment cameras when viewed from the upward-facing fisheye camera on the calibration robot.

The distributed camera system (Figures 1 & 3) comprises several static environment cameras which have minimal to no overlapping fields of view. They generate images of size 1080 x 1920 pixels at 30 Hz. We use the factory provided intrinsic calibration parameters for these cameras.

B. The Calibration Robot

We use a Clearpath Jackal as our calibration robot (Figure 2). The robot has a rigidly attached upward-facing wide-angle (160°) 2MP fisheye camera which generates images of size 1080 x 1920 pixels at 30 Hz. We face the fisheye camera upward because the ceiling (height varying between 3 - 4 m from ground level) of our indoor facility ensures the presence of sufficient static features to track for robot pose estimation using VO. We use a wide-angle lens for VO such that we can cover a large FoV and track several features. Moreover, a wide-angle camera ensures that several environment cameras can be detected (using OpenCV [20] blob detection, Figure 3), which we use to further constrain the position of the detected cameras in the estimation procedure. We use the fisheye camera calibration toolbox available in MATLAB [21] to obtain its intrinsics. A backlit ArUco marker [2] of known dimensions is attached to the calibration robot so that the robot can be easily detected by the environment cameras (Figure 4). The calibration robot also has a 64 Channel Ouster 3D-LiDAR which generates 3D scans at 10 Hz used for doing LiDAR Odometry (LO) [22] based calibration of environment cameras - a method we will compare our approach against.



Fig. 4: **Looking down ↓ Robot Detection from Edge Node:** The Calibration Robot viewed from an environment camera with axes drawn on the detected backlit ArUco marker.

C. Notation

In this work, 6-DoF pose is expressed as a homogeneous transformation matrix $T = \begin{bmatrix} R(q) & p \\ 0 & 1 \end{bmatrix}$, where rotation R is represented as quaternion q and position p as a $R^{3 \times 1}$ vector. The global frame W coincides with the origin of the robot motion estimated using VO. The pose T_F^W of the fisheye camera F is synonymous with the calibration robot pose. We have N cameras $\{C_k\}_{k=0:N-1}$ in the distributed environment camera system with corresponding global poses $\{T_{C_k}^W\}_{k=0:N-1}$. The detection of the ArUco marker M on the calibration robot in an environment camera C_k results in

ArUco detection pose measurement $T_M^{C_k}$ which represents the pose of the ArUco marker in camera C_k frame. The fisheye camera F and the ArUco marker M have a spatial offset T_M^F between them. The fisheye camera F detects and tracks point features (as pixels $\in R^2$) to do VO for robot pose estimation. The fisheye camera also detects environment cameras $\{C_k\}_{k=0:N-1}$ as 2-D pixel ($\in R^2$) measurements on its image plane which are ultimately used to constrain all variables optimized in the estimation process.

D. Time Synchronization

We synchronize all edge nodes using an NTP (Network Time Protocol) server. A central server is set up as the NTP server and all the edge nodes and the calibration robot use this server to sync their time as NTP clients. The resulting synchronization has an error in the range of 1 to 2 milliseconds on the client devices in relation to the time on the server. However, since the sensors themselves (cameras and LiDAR on the robot vs the environment cameras) are asynchronous (not triggered together and have different frame rates), there is a small variable error between images and scans captured. This variable error will have negligible impact on registration because the calibration robot is operated at speeds much lower than its top speed (2 m/s).

V. PROBLEM STATEMENT

The primary goal of this work is to determine the pose $\{T_{C_k}^W\}_{k=0:N-1} \in SE(3)$ of environment cameras $\{C_k\}_{k=0:N-1}$ (Figure 3) with respect to a global frame W . As the environment cameras share no or minimal FoV, the calibration robot's fisheye camera pose $T_F^W \in SE(3)$ and the constant spatial offset $T_M^F \in SE(3)$ between the fisheye camera F and the ArUco marker M also need to be estimated such that an ArUco detection pose measurement like $T_M^{C_k} \in SE(3)$ can be used to estimate $T_{C_k}^W$ - camera C_k 's global pose (since $T_{C_k}^W = T_F^W T_M^F (T_M^{C_k})^{-1}$).

VI. METHOD

We follow a 3 step approach to solve this problem, they are: (A) Estimate un-scaled robot motion T_F^W (and unscaled map $\{X_k \in R^3\}_{k=0:P-1}$ of 3D points from 2D feature detection and tracking) with the upward-looking fisheye camera F using Visual Odometry (VO) (Section VI-A), (B) Estimate the scale s of VO and the spatial offset T_M^F between the upward-looking fisheye camera F and the ArUco marker M using detection of ArUco marker in the environment cameras (Section VI-B), (C) Estimate the poses $\{T_{C_k}^W\}_{k=0:N-1}$ of the distributed environment cameras $\{C_k\}_{k=0:N-1}$ using two way measurements i.e. ArUco detection pose measurements from detection of ArUco marker in the environment cameras $\{C_k\}_{k=0:N-1}$ and their detection in the fisheye camera F (Section VI-C).

A. Estimate Motion of the upward-looking fisheye camera using Visual Odometry (VO)

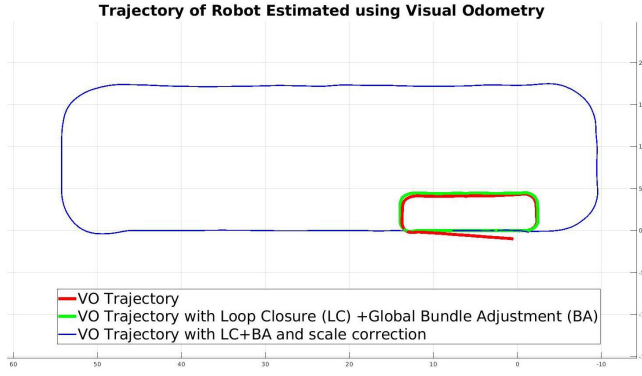


Fig. 5: **Motion estimation using Visual Odometry (VO).** The trajectory in red is the result from SVO [23]. We use loop closure [24] and bundle adjustment [25] to reduce the drift in VO (shown in green) and finally we determine the metric scale (in meters) (Section VI-B) of the trajectory using the detection of ArUco marker on the calibration robot.

We use SVO [23] to determine the frame to frame motion of the upward-looking fisheye camera on the robot. We choose SVO over other VO algorithms because of its ease of use and proven ability with wide-angle lenses [26]. Additionally, SVO can be optimized to work for downward-looking cameras in aerial robots where the camera tracks features on a dominantly flat surface, a situation which is similar to our case where we use an upward-looking camera that tracks static features on the ceiling. We eliminate drift in VO by implementing loop closure (using DBoW2 [24] for place recognition) and global bundle adjustment (in ceres solver [25]) using the reprojection error residual Equation 1 for the minimization problem in Equation 2. (Figure 5).

$$r_{kj} = \begin{bmatrix} u \\ v \end{bmatrix}_{kj} - \pi(K, T_{F_j}^W, X_k) \quad (1)$$

$$\begin{aligned} \{\hat{T}_{F_j}^W\}_{j=0:M-1}, \{\hat{X}_k\}_{k=0:P-1} = \\ \operatorname{argmin}_{\{T_{F_j}^W\}_{j=0:M-1}, \{X_k\}_{k=0:P-1}} \sum_{j=0}^{M-1} \sum_{k=0}^{N-1} w_{kj} \rho(\|r_{kj}\|^2) \quad (2) \end{aligned}$$

Here $w_{kj} = 1$ if 3D-point X_k is visible in the j^{th} robot keyframe otherwise $w_{kj} = 0$, $\rho()$ is Cauchy Loss Function for suppressing the effect of outliers in feature measurements. Here K & π are the intrinsic calibration parameters and the fisheye projection model respectively. We extract M robot keyframes (pose + image) from VO and use them in the loop closure and bundle adjustment process and in the next steps of the registration procedure. A comparison of trajectories before and after bundle adjustment is shown in Figure 5.

Because of the asynchronous nature of data generated from several sources we use pose interpolation to associate a robot pose to each ArUco detection. Without going into implementation details in the interest of space, consider a case when the ArUco detection has a timestamp $t \in (t_i, t_j)$ where t_i and

t_j are the timestamps of the robot keyframes F_i and F_j with poses $T_{F_i}^W = \begin{bmatrix} R(q_{F_i}^W) & p_{F_i}^W \\ 0 & 1 \end{bmatrix}$ and $T_{F_j}^W = \begin{bmatrix} R(q_{F_j}^W) & p_{F_j}^W \\ 0 & 1 \end{bmatrix}$ respectively, then the robot pose $T_F^W(t)$ at time t is determined by taking weighted average of $p_{F_i}^W$ & $p_{F_j}^W$ - for the translation component, and slerp (Spherical Linear Interpolation [27]) - for the rotation component. This method allows us to associate each ArUco detection $T_M^{C_k}(t)$ with an interpolated robot pose $T_F^W(t) \in SE(3)$. These interpolated poses will help us to determine the metric scale s of the robot trajectory from VO, the spatial offset T_M^F between fisheye camera F & ArUco marker M , and finally in estimating the environment camera poses $\{T_{C_k}^W\}_{k=1:L}$.

B. Determine the scale of VO & the spatial offset between the ArUco marker M and the upward-looking fisheye camera F using ArUco detections

We use the ArUco detection pose measurements $T_M^{C_k} \in SE(3)$ (this is the pose of the marker M in frame C_k) to determine the metric scale s of the trajectory estimated by monocular VO and the spatial separation T_M^F between the fisheye camera and the ArUco marker. The motion-based calibration technique [28] is employed for this purpose, using which we align the fisheye camera motion estimated by VO with the motion of the ArUco marker estimated by its detection in an environment camera C_k . For two adjacent robot keyframes F_i & F_{i+1} , we search for the nearest ArUco detection measurements $T_{M_i}^{C_k}$ & $T_{M_{i+1}}^{C_k}$ in the same environment camera C_k by comparing timestamps. Next, we use the previously described pose interpolation to determine the robot pose $\text{int } T_{F_i}^W$ & $\text{int } T_{F_{i+1}}^W$ corresponding to timestamps of ArUco measurements $T_{M_i}^{C_k}$ & $T_{M_{i+1}}^{C_k}$ respectively. Our goal is to align $\text{int } T_{F_{i+1}}^W (= (\text{int } T_{F_i}^W)^{-1} \text{int } T_{F_{i+1}}^W)$ with $T_{M_{i+1}}^{M_i} (= (T_{M_i}^{C_k})^{-1} T_{M_{i+1}}^{C_k})$ and in the process determine the metric scale s of robot trajectory and also the spatial offset T_M^F between the fisheye camera F and the marker M . We model the VO trajectory with a scale factor s multiplied to the translation component $\text{int } p_{F_{i+1}}^F$. We solve a non-linear least squares optimization problem to determine the unknown variables. The residual r_i for this optimization process is given by:

$$r_i = \text{int } T_{F_{i+1}}^F T_M^F \ominus T_M^F T_{M_{i+1}}^{M_i} \quad (3)$$

The symbol \ominus differentiates the operation from a standard subtraction in Euclidean space and is meant to demonstrate operations on manifolds. We model $\text{int } T_{F_{i+1}}^F = \begin{bmatrix} R(\text{int } q_{F_{i+1}}^F) & s \cdot \text{int } p_{F_{i+1}}^F \\ 0 & 1 \end{bmatrix}$. We use the ceres solver [25] to solve for s and T_M^F by minimizing a cost function as shown in Equation 4.

$$\hat{s}, \hat{T}_M^F = \operatorname{argmin}_{s \in R, T_M^F \in SE(3)} \sum_{i=0}^{L-1} \rho(\|r_i\|^2) \quad (4)$$

Here L is the number of motion segments and $\rho()$ is Huber Loss Function. The estimated scale s and spatial offset T_M^F

are used to re-scale VO pose estimates (Figure 5) and to estimate the environment camera poses (Section VI-C).

C. Estimate the poses of the environment cameras

1) *Looking Down*: We use the ArUco pose measurements from each environment camera of the distributed system to determine its pose in a global coordinate system. For a single camera C_k of the distributed system, we gather all the ArUco pose measurements $\{T_{M_i}^{C_k}\}_{i=0:N_k-1}$ which measure the poses of the ArUco marker in the camera C_k frame as the calibration robot drives under it, and use their respective timestamps to determine the corresponding robot/fisheye camera pose $\{\text{int } T_{F_i}^W\}_{i=0:N_k-1}$ using interpolation. For ArUco measurements $\{T_{M_i}^{C_k}\}_{i=0:N_k-1}$ from camera C_k , and the corresponding interpolated robot poses $\{\text{int } T_{F_i}^W\}_{i=0:N_k-1}$, the pose of environment camera C_k can be determined from Equation 5 by solving a non linear least squares optimization problem using ceres library [25].

$$\hat{T}_{C_k}^W = \underset{T_{C_k}^W \in SE(3)}{\operatorname{argmin}} \sum_{i=0}^{N_k-1} \rho(\|T_{C_k}^W T_{M_i}^{C_k} \ominus \text{int } T_{F_i}^W \hat{T}_M^F\|^2) \quad (5)$$

Here N_k is the number of ArUco detection pose measurements made by camera C_k and $\rho()$ is Huber Loss Function. We perform this optimization (Equation 5) for all environment cameras $\{C_k\}_{k=1:N}$ to estimate their respective 6-DoF pose using respective ArUco detection pose measurements made by looking down on the calibration robot driving below.

2) *Looking Up - Position Refinement*: In this step our goal is to refine the positions $\{p_{C_k}^W\}_{k=0:N-1} \in R^3$ of the estimated camera poses $\{T_{C_k}^W\}_{k=0:N-1} \in SE(3)$ by minimizing the re-projection error between the projection $\pi(K, T_{F_j}^W, p_{C_k}^W)$ of the estimated environment camera position $p_{C_k}^W$ and the corresponding pixel detection $\begin{bmatrix} u \\ v \end{bmatrix}_{kj}$ (obtained using OpenCV's blob detection algorithm) on the upward facing fisheye camera image. We associate $\pi(K, T_{F_j}^W, p_{C_k}^W)$ to $\begin{bmatrix} u \\ v \end{bmatrix}_{kj}$ by performing a nearest neighbour search. The residual for minimizing the re-projection error is given in Equation 6.

$$r_{kj} = \begin{bmatrix} u \\ v \end{bmatrix}_{kj} - \pi(K, T_{F_j}^W, p_{C_k}^W) \quad (6)$$

r_{kj} can be defined as the re-projection error of the k^{th} environment camera when viewed from the j^{th} robot key-frame pose. Here K & π are the intrinsic calibration parameters and the fisheye projection model respectively. We solve this minimization problem (Equation 7) using ceres library [25].

$$\{\hat{T}_{C_k}^W\}_{k=0:N-1} = \underset{\{T_{C_k}^W\}_{k=0:N-1} \in SE(3)}{\operatorname{argmin}} \sum_{j=0}^{M-1} \sum_{k=0}^{N-1} w_{kj} \rho(\|r_{kj}\|^2) \quad (7)$$

Here $w_{kj} = 1$ if environment camera C_k is visible in the j^{th} robot key-frame otherwise $w_{kj} = 0$ and $\rho()$ is Cauchy Loss Function.

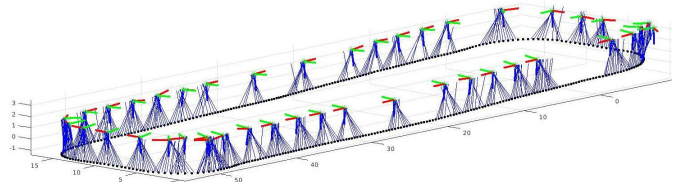


Fig. 6: Plot of estimated environment cameras and scaled robot/fisheye camera trajectory. The blue straight lines are robot-mounted ArUco marker detections from the environment cameras.

Figure 6 shows a plot of estimated variables and ArUco detection pose measurements.

VII. EXPERIMENTS & RESULTS

We collected two datasets by driving the calibration robot under a loop of several environment cameras of the distributed system. We calibrate 43 and 38 environment cameras in datasets 1 & 2 respectively. The images from its upward-looking fisheye camera are used to do VO, and the environment cameras detect the ArUco marker on the robot (Figure 4). Additionally, we also collect 3D scans from the LiDAR on the calibration robot for performing qualitative comparison of the proposed VO based solution against a LiDAR Odometry (LO) based approach. One of the immediate advantages of the VO based method over the LO based approach is that one can perform qualitative verification of environment camera registration by projecting them on the fisheye camera image.

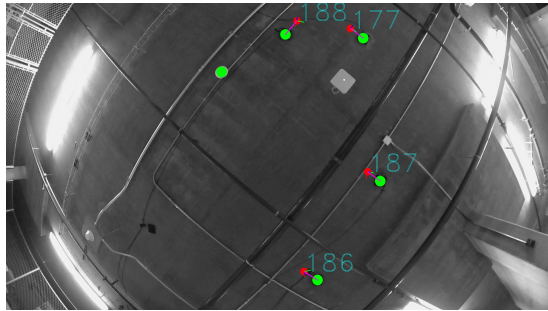
A. Verification using self contained methods

We present improvement in environment camera re-projection errors before (Section VI-C.1) and after (Section VI-C.2) refinement of estimated environment camera positions in Figures 7a & 7b and Table I.

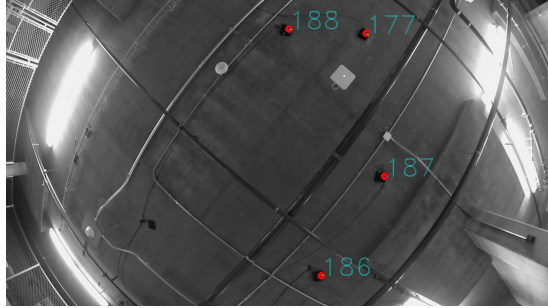
Reprojection Error (Pixel)		
	Before Refinement	Post Refinement
Dataset 1	51.642	10.428
Dataset 2	54.245	5.675

TABLE I: Root Mean Squared Re-projection Error calculated by measuring the re-projection error of the estimated distributed camera poses on each fisheye camera keyframe.

Clearly, the misalignment in the projection of estimated environment cameras and the corresponding detections (using OpenCV's blob detection) in the calibration robot's fisheye camera is significant before minimization of re-projection error (Figure 7a), whereas we see diminished misalignment after the optimization (Figure 7b). One of the reasons behind the misalignment (in Figure 7a) can be partial observability in solving for the spatial offset b/w fisheye camera and ArUco marker T_M^F in Equation 4 [29] resulting from planar robot motion. Since we cannot substantially improve T_M^F 's estimation owing to limitations on the range of motion the calibration robot can perform, we refine the environment camera positions by minimizing re-projection error instead of expending effort on improving T_M^F . The Figures 7a & 7b



(a) **Re-projection before camera position refinement.** The detected environment cameras (green) do not align with projection of environment cameras (red).



(b) **Re-projection after camera position refinement.** The projection of estimated environment cameras coincide with corresponding environment cameras on the fisheye image.

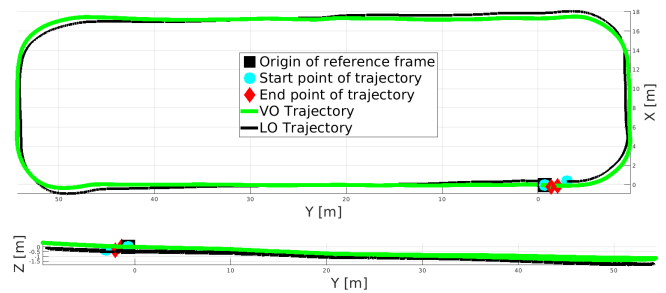
Fig. 7: Re-projection of distributed camera positions before and after re-projection error based refinement of camera positions.

show the qualitative result for just one robot-keyframe image. We present the root mean squared reprojection error (RMSE) over the entire robot trajectory for both the datasets in Table I, where we quantitatively show that the reprojection error post optimization is significantly smaller.

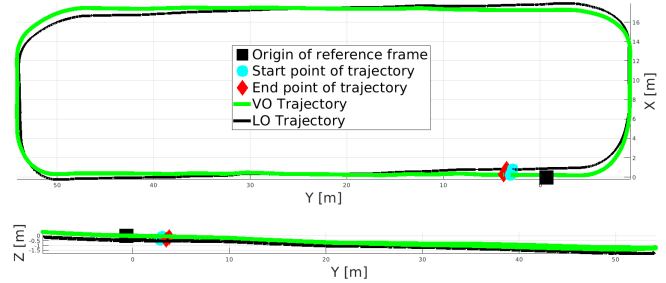
B. Comparison with Lidar Odometry (LO) based method

In the absence of ground truth, we compare our method against a LO based approach which uses LiDAR odometry instead of Visual Odometry (VO) to bridge environmental camera poses. A plot of the robot trajectories estimated by VO & LO for datasets 1 & 2 is presented in Figures 8a & 8b. We align the trajectories together by aligning the poses of the static environment cameras estimated by both the methods using a technique similar to [30]. The LO based approach determines robot trajectory by scan matching [22] and estimates the environment camera poses by minimizing a cost function with a residual similar to Equation 5. As LiDAR measures 3D points in metric units, it is not necessary to determine the metric scale of LO, but the spatial offset between the LiDAR and the ArUco marker is determined using motion based calibration [28] method discussed in Section VI-B.

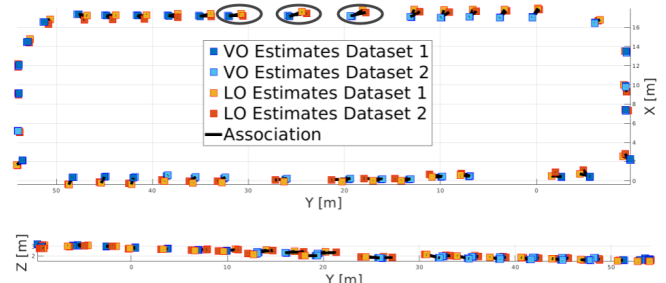
1) *LO - A brief explanation:* In short, the LO based approach is a Pose Graph Optimization based LiDAR pose estimation and mapping technique which we currently use to perform registration of the environment cameras.



(a) Top and side view of calibration robot trajectories estimated by VO & LO based methods for dataset 1.



(b) Top and side view of calibration robot trajectories estimated by VO & LO based methods for dataset 2.



(c) Top and side view of environment camera positions estimated by VO and LO based approaches for dataset 1 & 2. The ovals drawn around the top longer edge is to highlights the larger difference along Y – axis for the positions estimated from both methods across datasets.

Fig. 8: **VO vs LO:** Comparison of robot trajectories and estimated environment camera poses between the VO and LO methods. Both methods are represented in a common frame of reference.

2) *Evaluation:* Our goal is to discover if the VO based solution presented here gives comparable results. In order to compare the absolute environment camera poses we represent estimated variables in a common frame of reference. We choose the reference frame of the VO based solution from dataset 1 - W_1^{VO} as the reference for comparison. Next, we determine the transformations $T_{\chi}^{W_1^{VO}}$ to transform the environment cameras poses estimated in frames $\chi = \{W_2^{VO}, W_1^{LO}, W_2^{LO}\}$ to W_1^{VO} . These transformations are determined by minimizing the cost function in Equation 8 which is a method similar to [30] using ceres-solver [25].

$$\hat{T}^{W_1^{VO}} = \underset{T_{\chi}^{W_1^{VO}}}{\operatorname{argmin}} \sum_{k=0}^{N-1} \left\| T_{C_k}^{W_1^{VO}} \ominus T_{\chi}^{W_1^{VO}} T_{C_k}^{\chi} \right\|^2 \quad (8)$$

Here N is the number of common landmarks. We use the environment camera C_{ks} 's poses for determining $T_{\chi}^{W_1^{VO}}$ instead of aligning VO & LO trajectories because the cameras are static landmarks with unique ids that solve the data association problem across datasets and methods (VO/LO). Moreover, aligning trajectories involves matching timestamps which may not be accurate as the camera and LiDAR are not synced with each other. Using the estimated $T_{\chi}^{W_1^{VO}}$ we transform the environment cameras to a common frame of reference for comparing absolute environment camera poses. Visualization of the environment camera positions for both the approaches and both datasets is presented in Figure 8c. The RMS difference between corresponding

RMSE between corresponding environment cameras						
	ϕ°	θ°	ψ°	X[m]	Y[m]	Z[m]
$LO_1 \leftrightarrow VO_1$	3.7518	3.4510	3.0424	0.4509	0.6568	0.1388
$LO_1 \leftrightarrow VO_2$	3.2555	3.7371	2.7007	0.4625	0.7684	0.1375
$LO_2 \leftrightarrow VO_1$	3.5204	3.6040	3.6998	0.4095	0.8709	0.1328
$LO_2 \leftrightarrow VO_2$	3.1391	3.7304	2.0995	0.4371	0.9697	0.1330

TABLE II: RMSE for estimated env. camera poses between VO and LO based approaches for both the datasets. Here LO_i : environment cameras estimated from LO based approach in dataset i & VO_j : Corresponding environment cameras estimated from VO based approach in dataset j .

environment cameras poses estimated using both the VO based approach and the LO based approach for both the datasets are presented in Table II, where we observe that the RMS translation difference varies between 0.41-0.46 m along X axis and 0.1330-0.1388 m along Z axis, the difference is larger and varies between 0.66-0.97 m (a greater range) along Y axis. We observe in Figure 8c that the difference between the estimated environment camera poses between VO & LO across both the datasets is more along the longer edges of the elliptical trajectory. More specifically, the difference is larger at the top long edge with maximum misalignment being along Y axis as validated in Table II and highlighted ovals in Figure 8c. The maximum translational difference is ~ 1.08 m over a loop of 150-155 m and the maximum angular difference is 3.75° . As the difference is not systematic, one can attribute this to local measurement/estimation errors or local scale divergence in one or both the estimation techniques.

C. Repeatability of Results

In Figure 8c it can be observed that the environment camera estimates from the VO approach are bunched closer (light and deep blue squares) to each other than the estimates from the LO approach (light and deep orange squares). This is also quantified in Table III where the VO based estimates from both the datasets have lower RMS differences when compared against LO based estimates. This implies that the VO based approach gives more repeatable results than the LO based method.

VIII. DISCUSSION & CONCLUSION

We present a method to perform extrinsic calibration of a large network of environment cameras using a calibration

RMSE between corresponding environment cameras poses						
	ϕ°	θ°	ψ°	X[m]	Y[m]	Z[m]
$VO_1 \leftrightarrow VO_2$	0.0202	0.1010	0.0870	0.0838	0.1164	0.0379
$LO_1 \leftrightarrow LO_2$	0.0162	0.0069	0.0155	0.2749	0.4013	0.0446

TABLE III: RMS difference between corresponding environment cameras estimated from two different datasets using the same approach. We observe that the VO based method gives more repeatable results as evident from the lower RMSE.

robot equipped with an upward-facing fisheye camera and a backlit marker. We calibrate a loop of ~ 40 cameras in the perimeter of ~ 150 -155 m. We provide experimental results on two different datasets and compare our results with a LiDAR-based approach (LO). In contrast to LO, two-way sensing is possible with the visual approach, i.e. not only do the environment cameras detect the robot but the environment cameras are also detected in the robot's fisheye camera. This two-way sensing constrains the optimization better. The environment cameras also present unambiguous landmarks with no problems with data association between successive runs and can be used for downstream tasks like robot localization and navigation. The VO solution is not only comparable to LO, but also more repeatable (Table III). Moreover, the VO method also allows us to self-verify registration by projecting the estimated environment camera position onto the fisheye camera image (Figures 7a & Figures 7b). This is not possible in the LO approach. We also found experimentally that LiDAR scan matching and place recognition (for loop closure) is greatly affected in our facility with several dynamic objects around at all times. In contrast, an upward-facing camera mainly tracks static features on the ceiling unaffected by dynamic obstacles and more durable for long-term VO. Most importantly, a camera is smaller, lighter, cheaper, and consumes less power, making its use possible with cheaper robots. The limitation of the proposed approach is that the process does not determine the poses of exact camera centers, but since the re-projection of camera positions lies on the blobs associated with corresponding environment cameras and we know the dimensions of the environment camera nodes we have an upper bound on the uncertainty associated with the environment camera pose estimates.

In conclusion, our work presents large-scale calibration of a camera network with a mobile robot equipped with a single camera. Future work will explore the registration of a similar system with a camera-equipped drone and the use of such a system for the autonomous navigation of AVs, wheeled and flying robots.

REFERENCES

- [1] S. Gopalswamy and S. Rathinam, "Infrastructure enabled autonomy: A distributed intelligence architecture for autonomous vehicles," in *2018 IEEE Intelligent Vehicles Symposium (IV)*, pp. 986–992, 2018.
- [2] S. Garrido-Jurado, R. Muñoz-Salinas, F. J. Madrid-Cuevas, and M. J. Marín-Jiménez, "Automatic generation and detection of highly reliable fiducial markers under occlusion," *Pattern Recognit.*, vol. 47, pp. 2280–2292, 2014.
- [3] Y.-J. Cho and K.-J. Yoon, "Distance-based camera network topology inference for person re-identification," *Pattern Recognition Letters*, vol. 125, pp. 220–227, 2019.

[4] R. Farrell and L. S. Davis, "Decentralized discovery of camera network topology," in *2008 Second ACM/IEEE International Conference on Distributed Smart Cameras*, pp. 1–10, IEEE, 2008.

[5] P. Chakravarty and R. Jarvis, "External cameras and a mobile robot: A collaborative surveillance system,"

[6] Z. Zou, R. Zhang, S. Shen, G. Pandey, P. Chakravarty, A. Parchami, and H. X. Liu, "Real-time full-stack traffic scene perception for autonomous driving with roadside cameras," in *IEEE Int. Conf. Robot. Autom. (ICRA)*, 2022.

[7] S. Mishra, A. Parchami, E. Corona, P. Chakravarty, A. Vora, D. Parikh, and G. Pandey, "Localization of a smart infrastructure fisheye camera in a prior map for autonomous vehicles," in *IEEE Int. Conf. Robot. Autom. (ICRA)*, 2022.

[8] R. Xia, M. Hu, J. Zhao, S. Chen, Y. Chen, and S. Fu, "Global calibration of non-overlapping cameras: State of the art," *Optik*, vol. 158, pp. 951–961, 2018.

[9] D. Makris, T. Ellis, and J. Black, "Bridging the gaps between cameras," in *Proceedings of the 2004 IEEE Computer Society Conference on Computer Vision and Pattern Recognition, 2004. CVPR 2004.*, vol. 2, pp. II–II, 2004.

[10] A. Rahimi, B. Dunagan, and T. Darrell, "Simultaneous calibration and tracking with a network of non-overlapping sensors," in *Proceedings of the 2004 IEEE Computer Society Conference on Computer Vision and Pattern Recognition, 2004. CVPR 2004.*, vol. 1, pp. I–I, 2004.

[11] N. Anjum, "Camera localization in distributed networks using trajectory estimation," *J. Electrical and Computer Engineering*, vol. 2011, 01 2011.

[12] E. Ataer-Cansizoglu, Y. Taguchi, S. Ramalingam, and Y. Miki, "Calibration of non-overlapping cameras using an external slam system," in *2014 2nd International Conference on 3D Vision*, vol. 1, pp. 509–516, 2014.

[13] Y. Taguchi, Y.-D. Jian, S. Ramalingam, and C. Feng, "Point-plane slam for hand-held 3d sensors," in *2013 IEEE International Conference on Robotics and Automation*, pp. 5182–5189, 2013.

[14] H. Huang, N. Li, H. Guo, Y.-L. Chen, and X. Wu, "Calibration of non-overlapping cameras based on a mobile robot," in *2015 5th International Conference on Information Science and Technology (ICIST)*, pp. 328–333, 2015.

[15] F. Zhao, T. Tamaki, T. Kurita, B. Raytchev, and K. Kaneda, "Marker based simple non-overlapping camera calibration," in *2016 IEEE International Conference on Image Processing (ICIP)*, pp. 1180–1184, 2016.

[16] T. Pollok and E. Monari, "A visual slam-based approach for calibration of distributed camera networks," pp. 429–437, 08 2016.

[17] R. Mur-Artal, J. M. M. Montiel, and J. D. Tardós, "ORB-SLAM: a versatile and accurate monocular SLAM system," *CoRR*, vol. abs/1502.00956, 2015.

[18] K. Koide and E. Menegatti, "Non-overlapping rgb-d camera network calibration with monocular visual odometry," in *2020 IEEE/RSJ International Conference on Intelligent Robots and Systems (IROS)*, pp. 9005–9011, 2020.

[19] D. Scaramuzza and F. Fraundorfer, "Visual odometry [tutorial]," *IEEE Robotics Automation Magazine*, vol. 18, no. 4, pp. 80–92, 2011.

[20] G. Bradski, "The OpenCV Library," *Dr. Dobb's Journal of Software Tools*, 2000.

[21] D. Scaramuzza, A. Martinelli, and R. Siegwart, "A toolbox for easily calibrating omnidirectional cameras," in *2006 IEEE/RSJ International Conference on Intelligent Robots and Systems*, pp. 5695–5701, 2006.

[22] A. Segal, D. Hähnel, and S. Thrun, "Generalized-icp," 06 2009.

[23] C. Forster, M. Pizzoli, and D. Scaramuzza, "SVO: Fast semi-direct monocular visual odometry," in *IEEE Int. Conf. Robot. Autom. (ICRA)*, pp. 15–22, 2014.

[24] D. Gálvez-López and J. D. Tardós, "Bags of binary words for fast place recognition in image sequences," *IEEE Transactions on Robotics*, vol. 28, pp. 1188–1197, October 2012.

[25] S. Agarwal, K. Mierle, and T. C. S. Team, "Ceres Solver," 3 2022.

[26] Z. Zhang, H. Rebecq, C. Forster, and D. Scaramuzza, "Benefit of large field-of-view cameras for visual odometry," in *IEEE Int. Conf. Robot. Autom. (ICRA)*, 2016.

[27] K. Shoemake, "Animating rotation with quaternion curves," *SIGGRAPH Comput. Graph.*, vol. 19, p. 245–254, jul 1985.

[28] Z. Taylor and J. Nieto, "Motion-based calibration of multimodal sensor arrays," in *2015 IEEE International Conference on Robotics and Automation (ICRA)*, pp. 4843–4850, 2015.

[29] H. Chen, "A screw motion approach to uniqueness analysis of head-eye geometry," in *Proceedings. 1991 IEEE Computer Society Conference on Computer Vision and Pattern Recognition*, pp. 145–151, 1991.

[30] Z. Zhang and D. Scaramuzza, "A tutorial on quantitative trajectory evaluation for visual(-inertial) odometry," in *2018 IEEE/RSJ International Conference on Intelligent Robots and Systems (IROS)*, pp. 7244–7251, 2018.